

INVESTIGATING THE BINGGELI EFFECT: THE  
ALIGNMENT AND ORIENTATION OF BRIGHTEST  
CLUSTER GALAXIES WITH REDSHIFT USING HSC DATA



SAMUEL MOORE

ADVISED BY PROFESSOR MICHAEL STRAUSS

A SENIOR THESIS

SUBMITTED TO THE DEPARTMENT OF ASTROPHYSICAL SCIENCES  
IN PARTIAL FULFILLMENT OF THE REQUIREMENTS FOR  
THE DEGREE OF BACHELOR OF ARTS

PRINCETON UNIVERSITY

SPRING 2019

I hereby declare that I am the sole author of this thesis.

I authorise Princeton University to lend this thesis to other institutions or individuals for the purpose of scholarly research.

---

Samuel Moore

I further authorise Princeton University to reproduce this thesis by photocopying or by other means, in total or in part, at the request of other institutions or individuals for the purpose of scholarly research.

---

Samuel Moore

# Abstract

In this thesis, we examine the alignment between Brightest Cluster Galaxies (BCGs) and the orientation of their clusters. In particular, we are aiming to determine whether their alignment is dependent on redshift, which other studies (discussed in the introduction) have suggested. To do this, we use the Hyper Suprime-Cam (HSC) s18a v2 catalogue to analyse 13373 clusters at  $0.1 < z < 1.2$ . We then calculate the axial ratio and the orientation angle for both the BCGs and their host clusters. The initial results using these 13373 clusters show no correlation between alignment and redshift. We then impose certain criteria, selecting clusters with a large enough cluster size and a low enough redshift due to uncertainty in those objects ( $N > 30$ ,  $z < 0.8$ ), as well as the imposition that the BCG must have an axial ratio far enough from unity so that it has a well-defined orientation ( $\alpha < 0.8$ ). Doing so still reveals no evidence for alignment at all, and certainly no evidence for redshift dependence. We additionally find no correlation between dominance and alignment. Further work is recommended to assess if there are any statistical or technical problems that may be affecting these results, as well as a more thorough review of the prior evidence suggesting that there is a redshift dependence.

# Contents

<b>1</b>	<b>Introduction</b>	<b>1</b>
<b>2</b>	<b>Hyper Suprime-Cam</b>	<b>4</b>
<b>3</b>	<b>Analysis</b>	<b>9</b>
3.1	Cluster Parametrisation . . . . .	9
3.2	Cluster Parametrisation with Membership Probability . . . . .	12
3.3	Data Set Analysis . . . . .	13
3.4	Statistical Modelling of Clusters . . . . .	16
3.5	BCG Parametrisation . . . . .	19
3.6	Alignment . . . . .	23
3.7	BCG Dominance . . . . .	28
<b>4</b>	<b>Conclusions</b>	<b>30</b>
<b>A</b>	<b>Definition of <math>N_{cor}</math> and <math>w</math></b>	<b>32</b>

# Chapter 1

## Introduction

In this paper, we aim to investigate the relationship between the alignments of clusters and their Brightest Cluster Galaxies (BCGs). In particular, we wish to investigate whether there is an alignment between BCGs and their clusters (an effect known as the Binggeli effect), and to examine whether this alignment is redshift-dependent.

A typical BCG is located close to the centre of its host cluster, and hence probably lies at the bottom of the gravitational potential well of its cluster. BCGs have different properties from non-BCGs, for example, BCGs are larger and have higher velocity dispersions (Von der Lindern et al, 2007), exhibit photometric and colour homogeneity, have high luminosities  $\approx 10L_*$ , and often have disturbed morphologies. These differences suggest that the galaxy formation process differs between BCGs and non-BCGs.

The relationship between the orientation of Brightest Cluster Galaxies (BCGs) and that of the clusters over time is a significant aspect of understanding the cosmology of our universe. Various cosmological simulations indicate that there is a relationship between clusters and their constituent galaxies (Dubinski 1998), more specifically, predicting a relationship between their orientations. There are additionally a plethora of studies that there are alignments between other structures in the universe, including between galaxies and clusters (Hashimoto, Henry & Boehringer, 2008) and galaxies within groups (Wang et al. 2008).

There are two main hypotheses regarding the Binggeli Effect. The first argues that

it is a result of the formation process of BCGs and their clusters: both are formed in a preferred direction along filaments. The argument behind the first hypothesis stems from analysis of N-body simulations. For example, in Dubinski et al. (1998), an N-body simulation for galaxy merging generated a large central galaxy with surface brightness and velocity dispersion profiles similar to those of observed BCGs. The galaxy is a flattened, triaxial object whose long axis aligns with the primordial filament, suggestive that the alignment shouldn't change over time, and corresponds to predictions in prior papers. The second argues that tidal interactions cause the alignment of the BCG with the cluster. As noted by Ciotti & Dutta (1994), the timescale in which a galaxy is affected by the tidal field of its host cluster is far shorter than the Hubble time. This suggests that if tidal interactions play a significant role in aligning the BCG with its host cluster, then the alignment of the BCG will vary with respect to redshift. More specifically, one would expect the alignment to be weaker at higher redshift.

Former observational studies have demonstrated a relationship between the alignments of BCGs and clusters. The first example was Binggeli (1982). More recent studies have included Kim et al. (2002), Donoso et al. (2006), and Siverd et al. (2009), all of which have demonstrated evidence of the Binggeli effect to some degree. There are additionally a small number of early papers that suggest that there is no such alignment as suggested by Binggeli, such as Struble & Peebles (1985), instead suggesting that the effect may be explained by systematic errors. However, it is to be noted that the sample sizes used in these early papers is rather small; for instance, Struble & Peebles (1985) used a sample of 237 clusters. Another example of a paper that provided a negative result was Ulmer et al. (1989), which had similar shortcomings.

One of the most recent papers on this topic is Niederste-Ostholt et al. (2010), which uses SDSS Data Release 6 to study the alignment effect in 12755 clusters extending out to  $z = 0.44$  in order to show that BCGs are preferentially aligned. This study also investigates other aspects related to the Binggeli effect, concluding that rich clusters show a stronger alignment than do poor clusters at the  $2.3\sigma$  level; that low-redshift clusters (defined as  $z < 0.26$ ) show more alignment than do high-redshift ( $z > 0.26$ ) clusters, with a difference significant at the  $3.0\sigma$  level; and that there is a correlation between BCG dominance (defined as the difference in the magnitude of the BCG and the mean magnitude of the second and third-ranked galaxies) and cluster alignment. Using the recent data release from the Hyper

Suprime-Cam (HSC, discussed in Chapter 2), it is now possible to use a larger sample size with higher- $z$  clusters to provide further analysis of the Binggeli effect, up to approximately  $z = 1.2$ . This provides to us the opportunity to build upon the work of these prior papers.

One of the most recent demonstrations of the Binggeli effect that is relevant to this thesis was given by West et al. (2017). West et al. (2017) uses HST (Hubble Space Telescope) measurements of 65 distant clusters (up to  $z \approx 1.3$ ) and finds evidence for the alignment of BCGs and clusters. However, the authors do not find evidence for this alignment having any redshift dependence. Another useful paper is Donahue et al. (2016) who showed that BCG-cluster alignment is preserved independent of the means of measurement. More specifically, if the Binggeli effect was observed using gravitational lensing, then it was also observed using X-rays or the Sunyaev-Zel'dovich effect.

There is additionally a strong theoretical case for the Binggeli effect. Faltenbacher et al. (2002) used an N-body simulation with a  $\Lambda$ CDM model to show that the Binggeli effect is detected up to  $100h^{-1}\text{Mpc}$ . Furthermore, Onmora & Thomas (2000) used simulations of 5123 dark matter particles to investigate alignments of galaxies with their nearest neighbour galaxies, as well as between clusters within a supercluster. This paper found that under the  $\Lambda$ CDM framework, the Binggeli effect is present up to  $30h^{-1}\text{Mpc}$ . They also note that a diminished (i.e: holding for smaller distances) Binggeli effect is seen under alternative cosmological models, including tCDM, sCDM, and OCDM. Throughout this paper, we assume an  $\Omega_m = 0.28$ ,  $\Omega_\lambda = 0.72$  and  $H_0 = 70 \text{ km s}^{-1} \text{ Mpc}^{-1}$  cosmology (i.e: a flat  $\Lambda$ CDM cosmology) that is assumed in the production of the cluster catalogue used in this paper (Oguri et al. 2014). However, the  $\Lambda$ CDM parameters are not explicitly used in this thesis.

# Chapter 2

## Hyper Suprime-Cam

The Hyper-Suprime Cam (HSC) is a wide-field imaging camera on the 8.2m Subaru telescope located on Mauna Kea in Hawaii. The 1.5m diameter of the camera provides a large field of view ( $\approx 1.77 \text{ deg}^2$ ), whilst the location minimises any atmospheric disturbance because as it is at a higher altitude, there is less atmospheric turbulence occurring between the flux source and the telescope, reducing astrophysical 'seeing'. Additionally, the location of HSC near an ocean favours the generation of laminar flows over the mountain, which further reduces seeing, and reduces the problem of cloud cover. Overall, this makes HSC an excellent tool in astronomy for data collection.

The HSC survey is detailed extensively in Aihara et al. (2018). The survey comprises three layers: Wide, Deep and UltraDeep. In order to have a large sample size, this paper focuses on using data from the Wide Layer, which will cover  $1400 \text{ deg}^2$  in five bands: *grizy* (Oguri et al, 2018). *grizy* refers to the set of five broadband filters where each filter is designed to best observe a certain wavelength range. *g* and *r* correspond roughly to 'green' and 'red' wavelengths in the visible range of electromagnetic (EM) radiation, whilst *i*, *z*, and *y* correspond to parts of the near-infrared range of EM radiation. Figure 2.1 illustrates the coverage of the filters over the EM spectrum for HSC. As of the S18a release,  $305 \text{ deg}^2$  has been mapped in the Wide field.

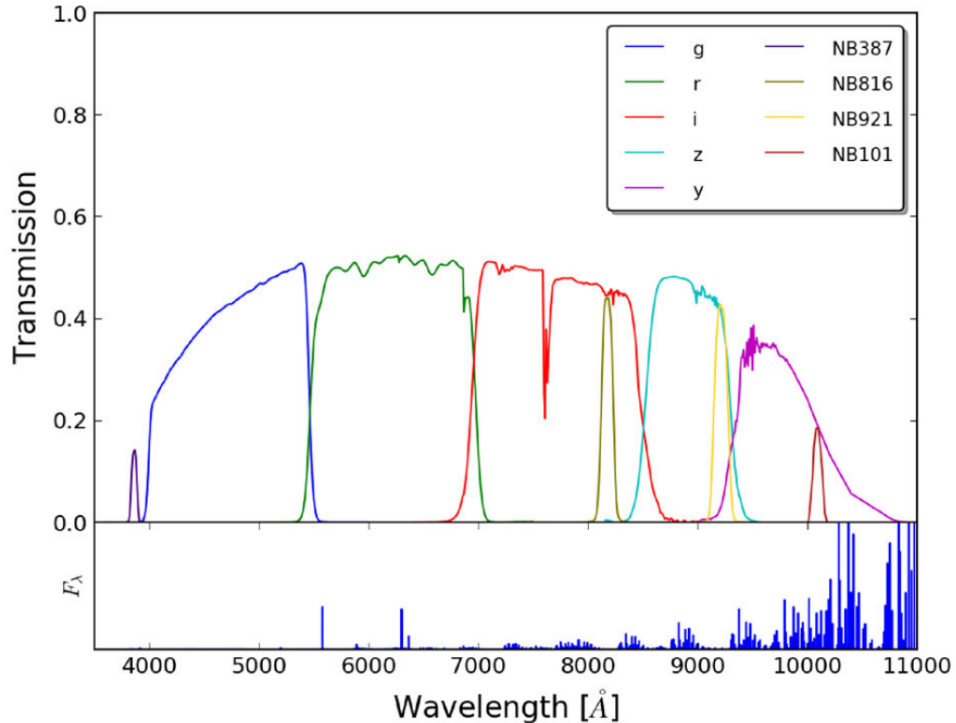


**Figure 2.1:** A figure showing the coverage of the grizy broadband filters for HSC, as well as 4 other narrow-band filters. The response of the five filters is given as a function of the wavelength, assuming an airmass of 1.2. Taken from Aihara et al. (2018).

The use of the HSC offers a number of advantages over previous surveys such as the SDSS. Primarily, using the Wide Layer of the HSC provides galaxy data up to  $z = 1.2$ , whereas the SDSS survey (as detailed in York et al., 2000) provided considerably less, up to  $z \approx 0.6$ . This is because the limiting magnitude of HSC in the Wide field is  $\approx 26$ , whereas for SDSS it is much lower at  $\approx 22.5$ , meaning that HSC is much more sensitive to fainter objects (which naturally tend to be at a higher redshift). Furthermore, the 'seeing' of HSC given by the Full-Width Half-Maximum (FWHM) is  $0.6''$ , compared to SDSS which is  $1.2''$ , which means that the images from HSC are of a higher resolution and thus HSC is better for distinguishing between two close objects.

In order to investigate the alignment of clusters and BCGs, we use the HSC s18a v2 catalogue compiled by Oguri et al. (2018). This catalogue is a set of 600333 galaxies making up 13373 distinct clusters, with a range  $0 < z < 1.2$ . The catalogue includes the Right Ascension and Declination (denoted RA and DEC in this paper respectively) of each galaxy and the RA and DEC of the central galaxy in the

cluster of that galaxy, which Oguri et al. (2014) considers to be the BCG. Additionally, values are given for the redshift ( $z$ ); the mask-corrected richness of the cluster ( $N_{cor}$ , as defined in Oguri et al. 2014);  $\log(M^*)$  which is the logarithm (base 10) of the mass of the galaxy in solar masses; and  $w$  the probability that a galaxy is a member of its catalogue cluster (also defined in Oguri et al. 2014).

For this catalogue,  $z$  is a photometric redshift. Whilst spectroscopic redshifts are far more precise, they are time-consuming to acquire, and thus impractical for large surveys such as HSC. Instead photometric redshifts are found, which measures the average intensity in different broad color filters (*grizy*) to obtain the redshift. Figure 2.2 gives the relationship between spectroscopic and photometric redshift values. They correlate well for the most part, showing that the measured photometric redshifts are a good measure of the actual redshifts of the galaxies, and thus are good for data analysis. However, this correlation weakens just above  $z \approx 0.8$  and thus we must be more cautious when drawing conclusions about trends at higher redshifts because these redshifts are less certain.

The precise definitions of  $N_{cor}$  and  $w$  given in Oguri et al. (2014) are relatively complicated. In brief,  $N_{cor}$  is a corrected measure of the richness of the galaxy which depends on factors such as the position and redshift of the galaxies, as well as a constraint on the mass of the galaxies to ensure the luminosity is not abnormally high or low, a constraint on the radial distance of galaxies from the centre to ensure galaxies are not too far away from the centre and that the number density falls away as a function of the radius, and a masking correction.  $w$  is a membership probability calculated with similar considerations, considering the number density parameter, mass and radius filters, and the distance of the galaxy from the BCG. For completeness, further explanations on the definitions are outlined in Appendix 1.

Cluster (28.657270, -4.618727)							
$RA_{cent}$	$DEC_{cent}$	$N_{cor}$	$z$	$RA_{gal}$	$DEC_{gal}$	$\log(M^*)$	$w$
28.657270	-4.618727	19.4040	0.564	28.668192	-4.657918	10.796	2.055799e-01
28.657270	-4.618727	19.4040	0.564	28.673328	-4.647884	10.803	3.367180e-01
28.657270	-4.618727	19.4040	0.564	28.668973	-4.637765	10.237	6.205157e-02
28.657270	-4.618727	19.4040	0.564	28.654660	-4.620519	10.388	1.00000e+00
28.657270	-4.618727	19.4040	0.564	28.674181	-4.666619	11.518	4.127302e-01
28.657270	-4.618727	19.4040	0.564	28.655106	-4.656679	10.494	6.518541e-02
28.657270	-4.618727	19.4040	0.564	28.664746	-4.653307	10.528	1.544849e-03
28.657270	-4.618727	19.4040	0.564	28.667236	-4.651917	10.049	5.614103e-03
28.657270	-4.618727	19.4040	0.564	28.671906	-4.650688	10.108	3.003528e-02
28.657270	-4.618727	19.4040	0.564	28.622938	-4.648751	10.739	9.959142e-02
28.657270	-4.618727	19.4040	0.564	28.669303	-4.642991	11.775	7.805720e-01
28.657270	-4.618727	19.4040	0.564	28.667946	-4.644180	11.416	9.054012e-03
28.657270	-4.618727	19.4040	0.564	28.673426	-4.644900	11.220	1.074490e-02
28.657270	-4.618727	19.4040	0.564	28.668912	-4.639457	11.077	9.263790e-01
28.657270	-4.618727	19.4040	0.564	28.672371	-4.643379	11.086	1.00000e+00
28.657270	-4.618727	19.4040	0.564	28.672256	-4.642879	10.529	5.133334e-01
28.657270	-4.618727	19.4040	0.564	28.669748	-4.642602	11.182	1.753872e-01
28.657270	-4.618727	19.4040	0.564	28.684918	-4.642483	10.908	4.998017e-01
28.657270	-4.618727	19.4040	0.564	28.674654	-4.641032	11.433	5.570905e-01
28.657270	-4.618727	19.4040	0.564	28.708402	-4.639560	10.850	8.993032e-03
28.657270	-4.618727	19.4040	0.564	28.636033	-4.638514	10.653	7.300468e-03
28.657270	-4.618727	19.4040	0.564	28.685163	-4.637590	10.398	5.200606e-02
28.657270	-4.618727	19.4040	0.564	28.670670	-4.638296	10.276	8.872315e-03

**Table 2.1:** This table lists the galaxies are given in the first cluster of the Oguri et al. catalogue. It shows the eight values given in the catalogue.

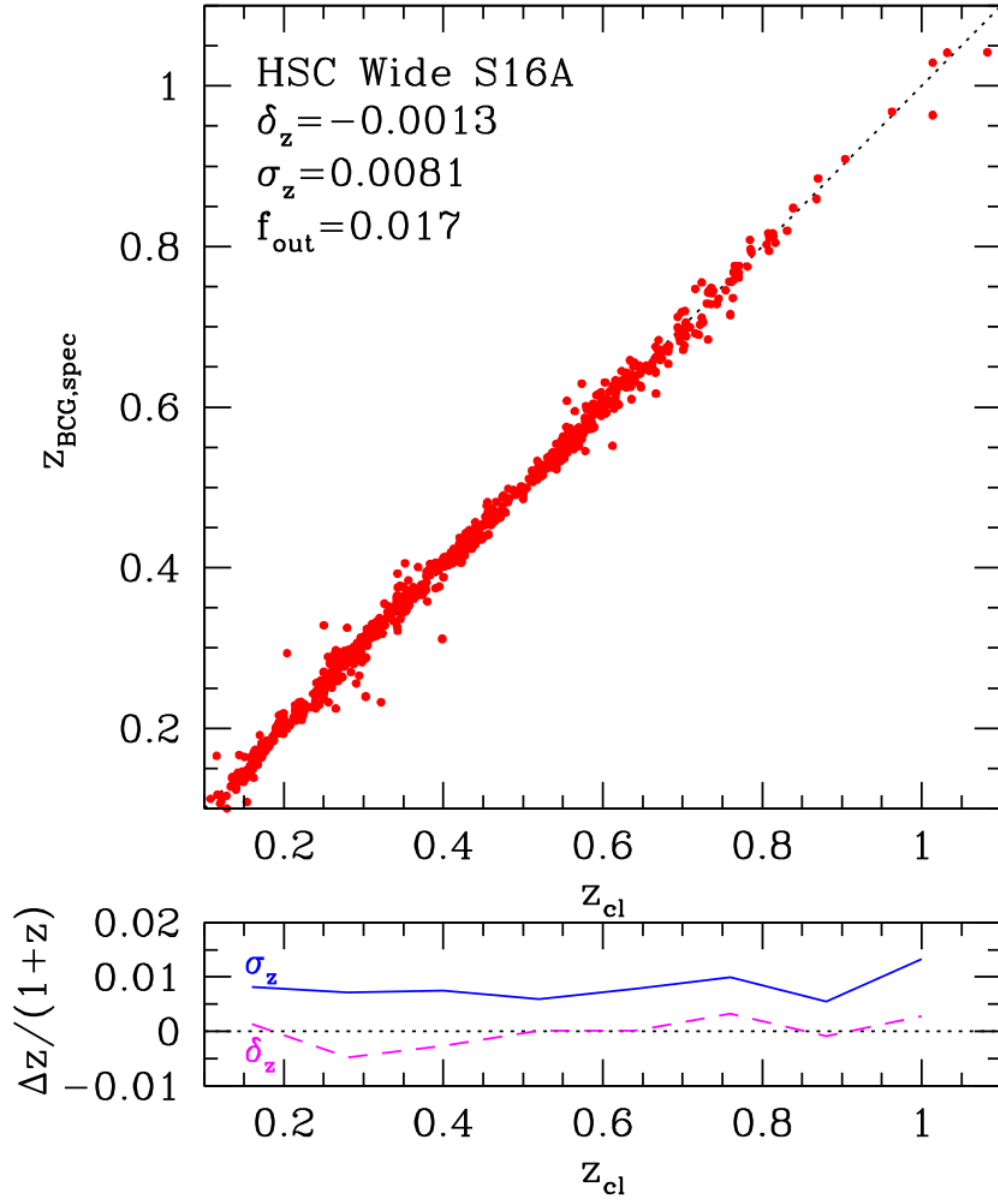


**Figure 2.2:** Taken from Oguri et al. (2016). (Top) This graph shows the relation between spectroscopic redshift ( $z_{BCG,spec}$ ) and photometric redshift ( $z_{cl}$ ). The motivation for this is as follows: In order to check the accuracy of  $z_{cl}$ , Oguri et al. (2016) cross-match the HSC Wide S116A cluster catalog with the spectroscopic galaxy catalogue to collect 843 clusters that have spectroscopic redshifts. By comparing the two redshift values, Oguri et al. (2016) find that the photometric redshift values are accurate because they are similar to the spectroscopic redshift values, although it should be noted that the uncertainty increases with higher photometric redshift. (Bottom) This graph gives the residual  $\frac{z_{cl} - z_{BCG,spec}}{1 + z_{BCG,spec}}$  for all clusters to find the bias and scatter, denoted  $\delta_z$  and  $\sigma_z$  respectively. For the s16a data, Oguri et al. (2016) finds values of  $\delta_z = -0.0013$ ,  $\sigma_z = 0.0081$ . One should note that the s18a data set is simply a larger data set that includes the s16a data set, which suffers from the same uncertainty in redshift.

# Chapter 3

## Analysis

### 3.1 Cluster Parametrisation

The position of each galaxy in each cluster is given by its Right Ascension (RA) and Declination (DEC), as shown in Table 2.1. In order to calculate values for the axial ratio ( $\alpha$ ) and angular orientation ( $\phi$ ) of a cluster, it is necessary to convert from (RA, DEC) to an (x,y) coordinate system, in essence mapping the celestial sphere onto a flat surface. For simplicity, when analysing each cluster, we set the cluster centre as the origin (x=0, y=0). To do this, one can simply map DEC  $\rightarrow$  x. However, one must introduce a correction factor when mapping RA  $\rightarrow$  y, as one is mapping a non-Euclidean surface to a Euclidean surface. As such, the conversion for each cluster is as follows:

$$x = (RA - RA_{mean}) \cdot \cos(DEC_{mean}) \quad (3.1)$$

$$y = DEC - DEC_{mean} \quad (3.2)$$

where, for  $i = 1, 2, \dots, n$

$$RA_{mean} = \frac{\sum_{i=1}^n RA_i}{n}$$

$$DEC_{mean} = \frac{\sum_{i=1}^n DEC_i}{n}$$

With the coordinate conversion complete, we can begin to find  $\alpha$  and  $\phi$  of each cluster. To do this, we follow the method utilised by both Kim et al. (2002) and Niederste-Ostholt et al. (2010), which use the principle of second moments to find  $\alpha$  and  $\phi$ .

$$M_{xx} = \left\langle \frac{x^2}{r^2} \right\rangle \quad (3.3)$$

$$M_{xy} = \left\langle \frac{xy}{r^2} \right\rangle \quad (3.4)$$

$$M_{yy} = \left\langle \frac{y^2}{r^2} \right\rangle \quad (3.5)$$

where  $x$  and  $y$  represents the respective distances of a given member galaxy from the cluster centre defined in the equatorial coordinate system, and  $r^2 = x^2 + y^2$ . One can then define the Stokes parameters as follows to find  $\alpha$  and  $\phi$ :

$$Q = \frac{1 - \alpha}{1 + \alpha} \cos(2\phi) = 2M_{xx} - 1 \quad (3.6)$$

$$U = \frac{1 - \alpha}{1 + \alpha} \sin(2\phi) = 2M_{xy} \quad (3.7)$$

From this, if one defines  $D = \sqrt{Q^2 + U^2}$ , one can calculate  $\alpha$  and  $\phi$  as follows:

$$\alpha = \frac{1 - D}{1 + D} \quad (3.8)$$

$$\phi = \frac{1}{2} \arctan\left(\frac{U}{Q}\right) \quad (3.9)$$

One should note that there is a degree of uncertainty in these measurements. For instance, the uncertainty in  $Q$  and  $U$  is given by:

$$\sigma_Q = \sqrt{\frac{2}{N(N-1)} \Sigma \left( \frac{x^2}{r^2} - \left\langle \frac{x^2}{r^2} \right\rangle \right)^2} \quad (3.10)$$

$$\sigma_U = \sqrt{\frac{2}{N(N-1)} \sum \left( \frac{xy}{r^2} - \left\langle \frac{xy}{r^2} \right\rangle \right)^2} \quad (3.11)$$

Additionally, it is necessary to standardise the angle of the cluster and the angle of the BCG such that they are both measured from the same half-line. We take the East direction to be the half-line at which  $\theta = 0$ , with an angle range from  $0 < \theta < 180$ . Note that this only goes through half a circle due to redundancy (i.e. an angle from -180 to 0 is expressible as a corresponding angle from 0 to 180 from the other side).

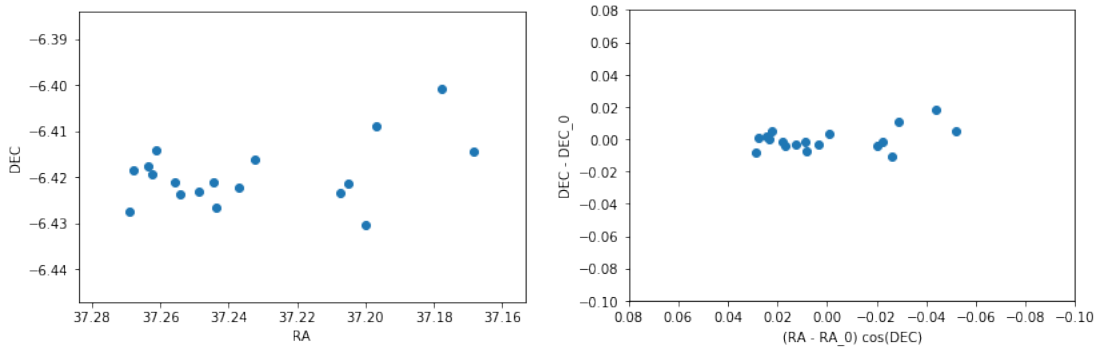


**Figure 3.1:** (Left) An example of a plotted cluster map,  $(RA, DEC) = (37.20747, -6.423215)$ . Here we are plotting the positions of each galaxy of the cluster. One should note that this is a particularly elongated cluster, and Figure 3.6 will later show that this is not the norm; the majority of clusters are relatively well-rounded. Looking at elongated clusters can be particularly useful as it is easy to judge the value of  $\phi$  by eye, and thus check if the code to calculate  $\phi$  is returning the correct value. (Right) The same cluster map with the Euclidean correction, now centered at the origin. For this cluster, we calculate  $\alpha = 0.14546$ ,  $\phi = 171.6^\circ$ .

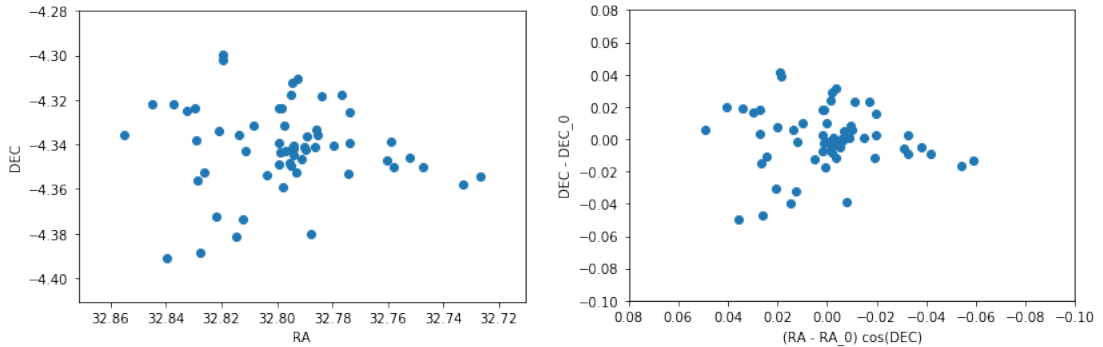


**Figure 3.2:** For completeness, the above maps show a rounded cluster, which is more commonly seen in the data set. The RA-DEC coordinates for this cluster are  $(32.79381, -4.344772)$ , and we calculate  $\alpha = 0.84817$ ,  $\phi = 11.4^\circ$ . (Left) Before the Euclidean transform. (Right) After the Euclidean transform.

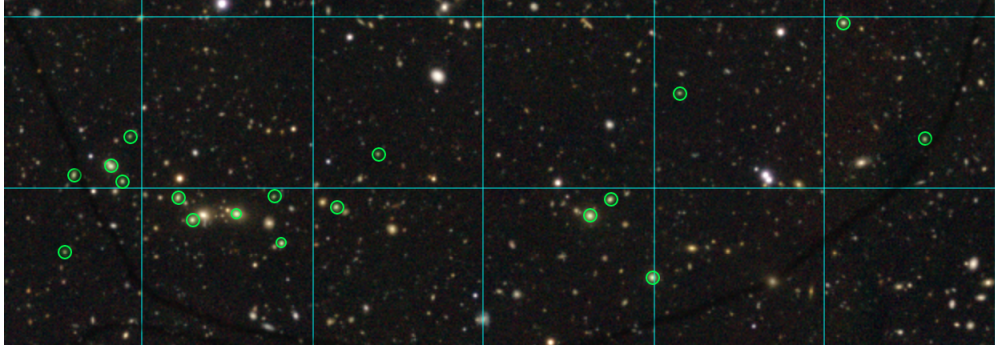


**Figure 3.3:** This shows the HSC Map centered on the cluster at (37.20747, -6.423215). The HSC map is a colour-corrected map with all images in this paper being a composite of exposures in three filters: g, r, i. Here, the members of the cluster are indicated with green circles. This matches with the positions found in Figures 3.1 and 3.2, and is a useful check that the code is functioning correctly.

## 3.2 Cluster Parametrisation with Membership Probability

We calculate two values for  $\alpha$  and  $\phi$ , the first set without using the membership probability ( $w$ ) as weights, as detailed above. The second set uses the membership probability as weights in order to avoid significant distortion of results from galaxies with a low probability of being in the cluster. The methodology is similar to the above unweighted method, expect for the following:

Firstly, the calculation of the arithmetic mean is altered to include the weights, as follows:

$$RA_{mean} = \frac{\sum_{i=1}^n RA_i \cdot w_i}{\sum w_i}$$

$$DEC_{mean} = \frac{\sum_{i=1}^n DEC_i \cdot w_i}{\sum w_i}$$

Additionally, the moments are also calculated to include the weights:

$$M_{xx} = \frac{\sum \frac{x^2}{r^2} \cdot w_i}{\sum w_i} \quad (3.12)$$

$$M_{xy} = \frac{\sum \frac{xy}{r^2} \cdot w_i}{\sum w_i} \quad (3.13)$$

$$M_{yy} = \frac{\sum \frac{y^2}{r^2} \cdot w_i}{\sum w_i} \quad (3.14)$$

The Stokes parameters are then calculated in the same way as detailed above, and so are  $\alpha$  and  $\phi$ . In cases where there is ambiguity, we denote unweighted alpha as  $\alpha$ , and weighed alpha as  $\alpha_w$ . The same convention applies for  $\phi$  and  $\phi_w$ .

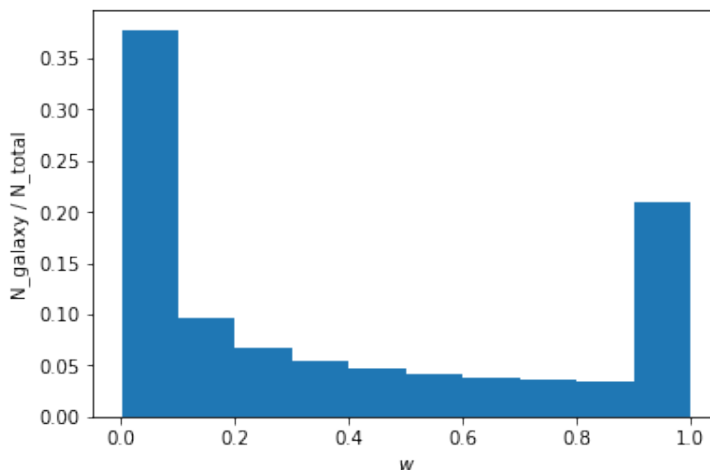


**Figure 3.4:** This is a histogram of the probability weights ( $w$ ) given by the Oguri catalogue. As shown, there are a large number of galaxies that have a very low-probability of being in the cluster (  $0 \leq w \leq 0.1$  ). To deal with these objects, we use the weighted method as discussed in Section 3.2.)

The motivation for using the weights comes from Figure 3.4, which shows a high number of low probability galaxies in the cluster catalogue. By using the weighted approach, we minimise the possibility that low probability galaxies could affect the values of  $\alpha$  and  $\phi$ .

### 3.3 Data Set Analysis

First of all, it is useful to conduct analysis upon the cluster catalogue itself to understand its various properties and to see if they conform to our expectations.

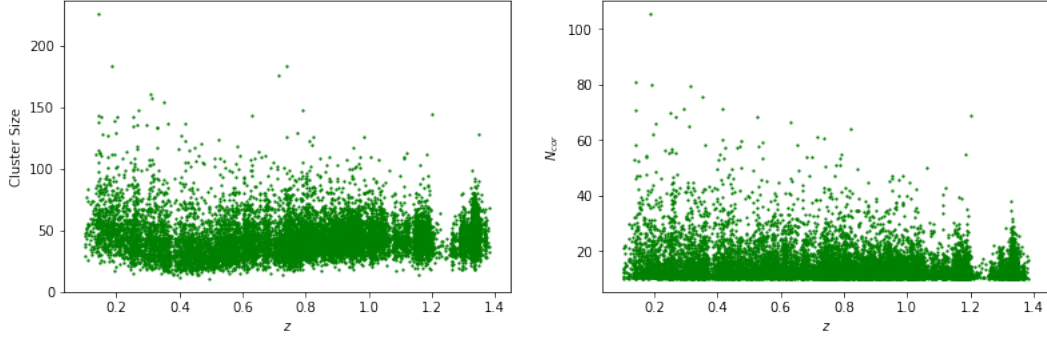


**Figure 3.5:** (Left) A scatter plot showing the relationship between the cluster size, and its redshift. The cluster size here is defined as the number of galaxies in each cluster, with no other correction. The probability weights are not used in the consideration of cluster size. Regression analysis indicates that the cluster size decreases with increasing redshift. (Right) A scatter plot showing the relationship between  $N_{cor}$  and  $z$ .

For this data set, the cluster size approximately decreases with increasing  $z$  (Fig. 3.5), although this decrease is rather modest. For clarity, cluster size is defined here simply as the number of galaxies in a given cluster, with no consideration of the probability weights.

Additionally, one can observe from Figure 3.6-3.8 various features regarding the axial ratio of the clusters against the cluster size, against  $N_{cor}$ , and a comparison of the weighted axial ratio vs. the regular axial ratio. One notes that there are a number of very elongated clusters ( $\alpha < 0.3$ ) shown in these figures. However, these low- $\alpha$  clusters tend to have a low sample size which is to be expected, as for a low sample size it is more likely that an individual galaxy in the cluster can distort the elliptical shape of the cluster significantly, making it more elongated. Furthermore, examining some of these clusters using the HSC map shows that these clusters are indeed elongated (such that the values of  $\alpha$  seem by eye to be correct). The same general principles outlined above can be applied to the  $N_{cor}$  graphs as well, suggesting that there are no problems with these graphs.

However, Figure 3.8 shows that there is can be a significant difference between the value of  $\alpha$  and the value of  $\alpha_w$  for a cluster. This suggests that there are a large number of clusters where galaxies with a low-probability ( $w < 0.5$ ) of being in the cluster are affecting the shape of the cluster significantly. This implies that using the weighted approach is better for our data analysis.

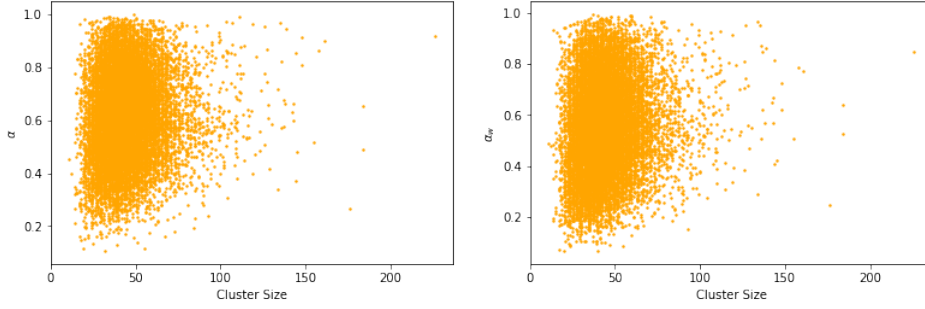


**Figure 3.6:** Graphs showing the size of each cluster against  $\alpha$  and  $\alpha_w$ . The graphs indicate that in both methods of calculating  $\alpha$ , there are few clusters that are very elongated ( $\alpha < 0.3$ ). Furthermore, those elongated clusters tend to be of a low cluster size. There is no drastic change between the graphs when the weighting by probability  $w$  is implemented.

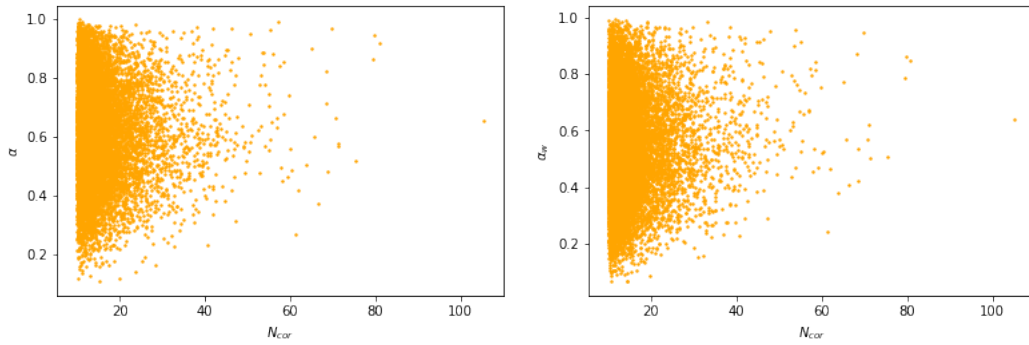


**Figure 3.7:** Graphs showing the  $N_{cor}$  value from the Oguri catalogue for  $\alpha$  and  $\alpha_w$ .  $N_{cor}$  is effectively another measure of cluster size with some corrective factors. We note that nothing seems problematic in these graphs.

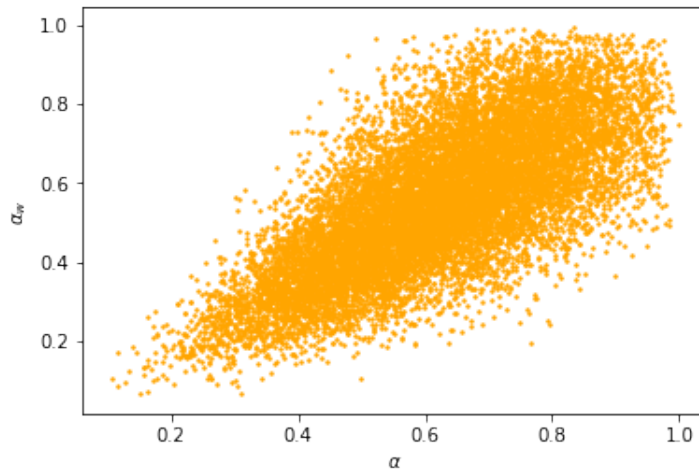


**Figure 3.8:** A plot showing  $\alpha$  vs.  $\alpha_w$  (weighted). This shows more clearly the difference between the two graphs in Figure 3.5. There will clearly be a difference in results throughout this paper based on whether the probability weights are used.

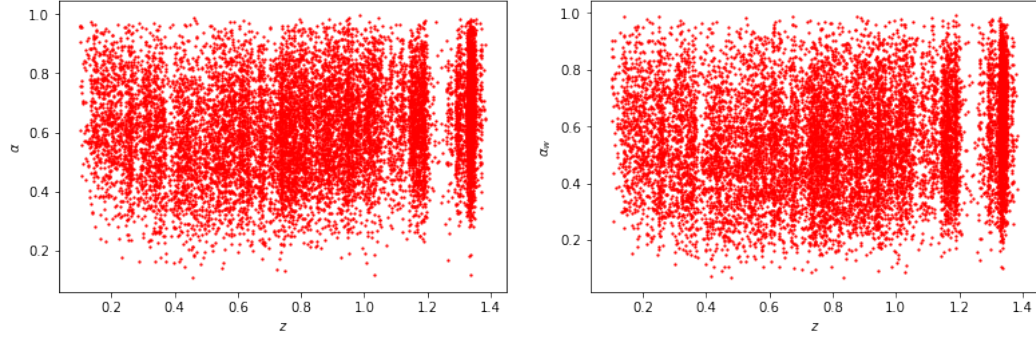


**Figure 3.9:** (Left) The scatter graph shows the distribution of the axial ratio of each cluster over redshift. (Right) The graph shows the distribution of the weighted axial ratio of each cluster over redshift. Regression analysis for both ratios indicates that there is a positive correlation between the axial ratio and redshift. Additionally, one ought to notice the high-density regions of clusters at high redshift (near  $z \approx 1.2$  and  $z \approx 1.4$ . It is odd to suddenly find a much larger number of clusters at high redshifts, which raises the question of how certain we are of their accuracy (i.e: are they actually at these redshift values?).

Figures 3.9a and 3.9b show scatter plots of  $\alpha$  vs.  $z$ , and  $\alpha_w$  vs.  $z$  respectively. In order to investigate the evolution of the elongation of clusters over time, we split the data into two sets: Low- $z$  ( $z < 0.6$ ), and high- $z$  ( $z > 0.6$ ). Figure 3.10a shows a histogram of the two data sets for  $\alpha_w$ , and Figure 3.10b shows the same data as a cumulative distribution function. The Kolmogorov-Smirnov test can be used to determine if two data sets are drawn from the same sample. Application of the Kolmogorov-Smirnov test in the case of  $\alpha$  gives: statistic = 0.0939, p-value =  $6.7187 \times 10^{-21}$ , while application of the test for  $\alpha_w$  gives: statistic = 0.0623, p-value =  $2.0153 \times 10^{-09}$ . In both cases, the p-values are exceptionally small, and far smaller than 0.01 (for a 99% confidence level). As a result, the difference between the low- $z$  distribution and the high- $z$  distribution is statistically significant. This indicates that the elongation of clusters varies over time, with  $\alpha/\alpha_w$  decreasing over time.

### 3.4 Statistical Modelling of Clusters

As a brief exercise to better understand the statistics behind  $\alpha$  and  $\phi$ , we carried out a number of exercises to observe how these values would change given the sample size of the cluster.

To begin with, we randomly selected a set number of points from a circle, which has a true value of  $\alpha = 1$ . We then calculated  $\alpha$  and  $\phi$  values for this theoretical cluster,

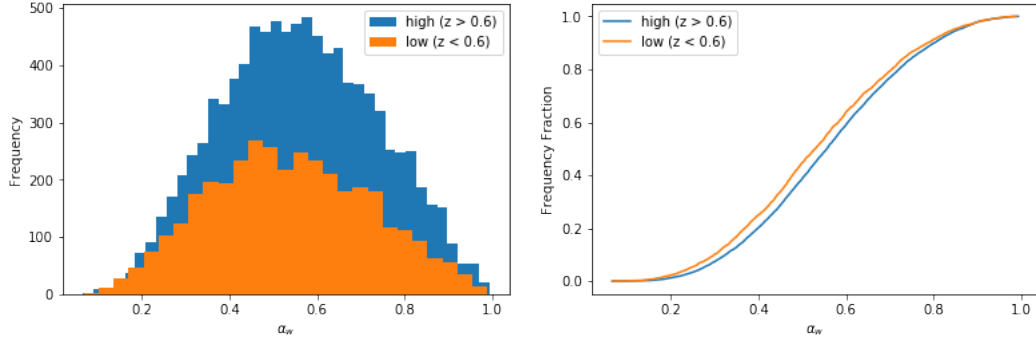


**Figure 3.10:** (Left) This figure shows a histogram of frequencies for  $\alpha_w$  when the data is divided into low- $z$  and high- $z$  (cut-off,  $z = 0.6$ ). (Right) This figure shows the same data represented as a normalised cumulative function. These graphs indicate that there is a difference between the distribution of  $\alpha_w$  for the two redshift groups.

before repeating this process a large number of times (10000). Figure 3.11 shows the results of plotting the distribution of  $\alpha$  and  $\phi$  for clusters of sample size 20, 25, and 30. As expected, as the sample size increases, the alpha value tends towards 1, but sees a reduced standard deviation when the sample size is increased, and the phi value is flat overall. One should note that the alpha distribution does not act as a normal distribution in this case. This is because the alpha distribution is bounded at its expected value of 1. As a result, the error from sampling pushes the average alpha value down. As a more clear demonstration of the value of alpha tending to 1, Figure 3.12 shows the alpha distribution for 150 trials with clusters of a sample size of 20000. The phi distribution is uniform (albeit with a large degree of noise due to fine binning) because there is no preferential angle when randomly selecting clusters in a circle.

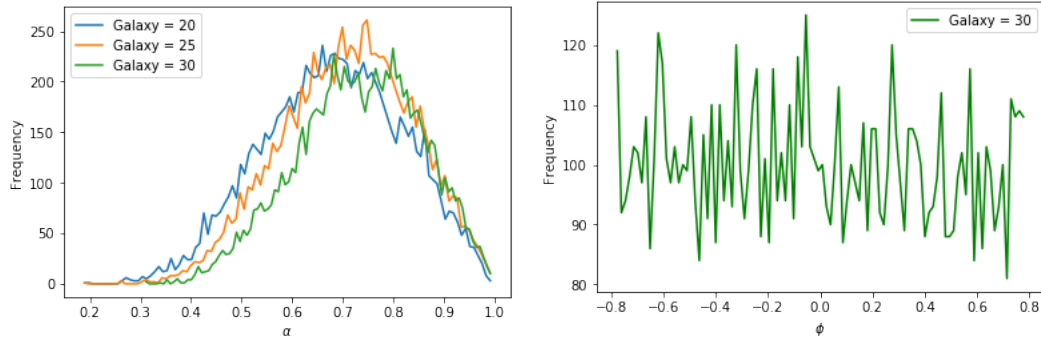


**Figure 3.11:** (Left) The graph shows the distributions of alpha values for a theoretical circular cluster for varying cluster sizes. (Right) The graph shows the same information, but for phi values (in radians) instead. (Trials = 10000). The alpha graphs show a distribution that is close to Gaussian (but with some skew), whereas the phi graph while noisy has a uniform distribution, with both distributions expected. For the sake of clarity, only the results for a sample size of 30 have been plotted for the phi modelling, however, the graph is also flat overall for the sample sizes 20 and 25 as well.

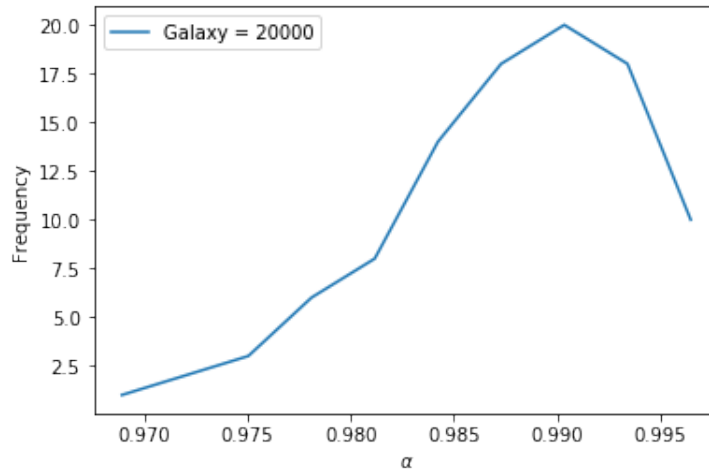


**Figure 3.12:** This figure demonstrates that as the sample size goes up, the value of  $\alpha$  tends towards 1. (Trials = 150)

This modelling test was repeated, this time picking from an ellipse in which the semi-major axis was twice as long as the semi-minor axis, resulting in alpha having an expected value of 0.5. Figure 3.13 shows the results of this test.

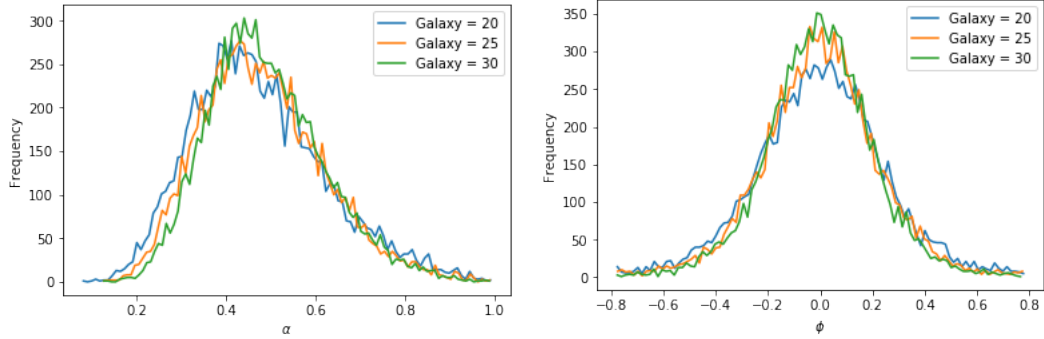


**Figure 3.13:** These figures show the alpha and phi distributions for elliptical sampling (trials = 10000). The alpha graphs show a distribution that is close to Gaussian (but with some skew). In addition, the phi graph is also Gaussian because there is now a preferred direction due to the shape of the ellipse being orientated with the semi-major axis along the x-axis (which contains the half-line  $\theta = 0$ ).

As shown, as the sample size increases, the alpha distribution tends towards the true value of 0.5, while the standard deviation of the values in both  $\alpha$  and  $\phi$  decreases.

The results of this test are significant in understanding the effects of shot noise on the data set. Shot noise can dominate when the sample size is sufficiently small so that uncertainties due to the Poisson distribution become significant. From this, it is recommend that we impose a minimum cluster size to conduct any analysis.

### 3.5 BCG Parametrisation

The next stage is to analyse the shape of the BCG. To do this, we use the CModel method as detailed in Bosch et al. (2017). The CModel method works by first fitting an ellipse to the image of a galaxy with a Sersic Model which is defined as:

$$\ln I(R) = \ln I_0 - kR^{\frac{1}{n}} \quad (3.15)$$

The Sersic model thus gives a relationship between the intensity of a galaxy,  $I$ , and the distance from its centre,  $R$ .  $n$  is a parameter that may be varied to give different profiles (and thus fit different galaxies); as  $n$  increases, the more the intensity falls off with distance.

In this case, the CModel method begins with an  $n = 1$  Sersic model (exponential),

which is often a reasonable approximation for the disc component of spiral galaxies. Next, it fits an ellipse with an  $n = 4$  Sersic Model (de Vaucouleurs) which is a reasonable approximation for elliptical galaxies. In both cases, the ellipse parameters are kept free. Then, both models are fitted at the same time, allowing only the two amplitudes to vary.

Let us define for the purposes of the CModel method, that  $A$  is the semi-major radius of the galaxy,  $B$  is the semi-minor axis, and  $\theta$  is the position angle. Then the CModel method returns a parametrisation of  $(A, B, \theta)$  by means of a symmetric positive-definite 2x2 matrix  $Q$ , which in terms of the HSC data set should be considered as:

$$Q = \begin{bmatrix} e_{11} & e_{12} \\ e_{12} & e_{22} \end{bmatrix} \quad (3.16)$$

As detailed in Bosch et al. (2017), the CModel matrices can be diagonalised as:

$$Q = \begin{bmatrix} \cos(\theta) & \sin(\theta) \\ -\sin(\theta) & \cos(\theta) \end{bmatrix} \begin{bmatrix} A^2 & 0 \\ 0 & B^2 \end{bmatrix} \begin{bmatrix} \cos(\theta) & -\sin(\theta) \\ \sin(\theta) & \cos(\theta) \end{bmatrix} \quad (3.17)$$

Noting that  $A^2$  and  $B^2$  then correspond to the eigenvalues of the CModel matrix, it is then trivial to calculate  $\alpha_{BCG} = \frac{A}{B}$  where  $A < B$ . Furthermore, it is clear that the eigenvectors of  $Q$  form the columns of the rotation vectors, allowing one to calculate  $\phi_{BCG}$ . It should be noted that in this case the cluster angle and the BCG angle are defined with respect to different  $\theta = 0$  half-lines, and thus it is necessary to correct for this. For the sake of clarity, from now on  $\alpha_{cluster} = \alpha_w$  and  $\phi_{cluster} = \phi_w$ .

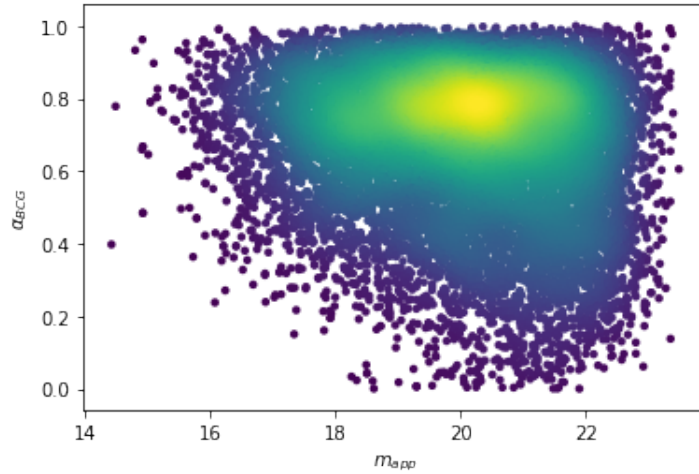


**Figure 3.14:** This contour plot shows  $\alpha_{BCG}$  against apparent magnitude. One should note that the vast majority of the elongated BCGs are at fainter magnitudes.

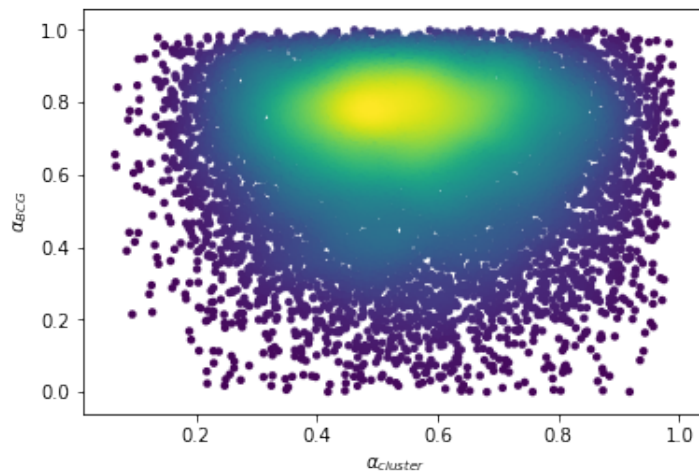


**Figure 3.15:** This contour plot shows  $\alpha_{BCG}$  against  $\alpha_{cluster}$ . There is no obvious correlation to be seen here.

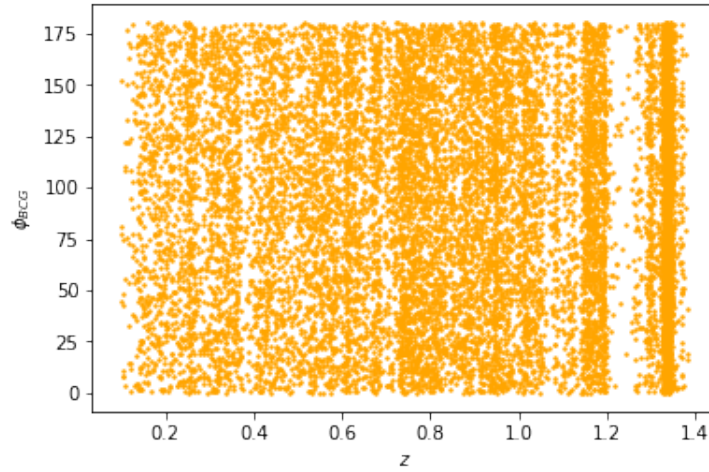


**Figure 3.17:** This scatter plot shows  $\phi_{BCG}$  against redshift.

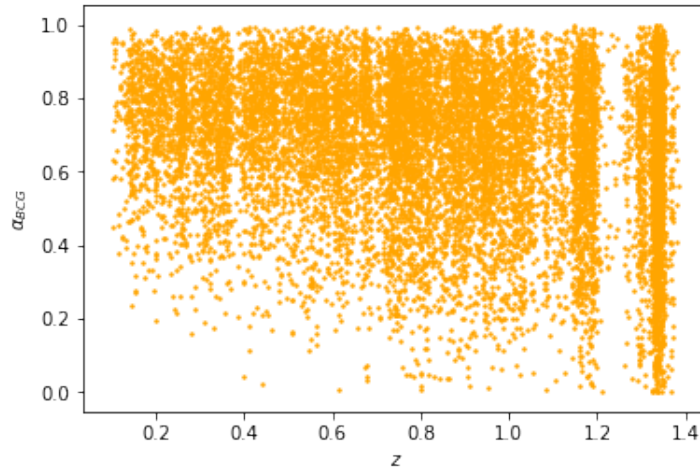


**Figure 3.16:** This scatter plot shows  $\alpha_{BCG}$  values against redshift. Here we note that the most elongated BCGs (i.e. BCGs with small  $\alpha$ ) tend to be at high redshift, which in turn tend to be fainter.

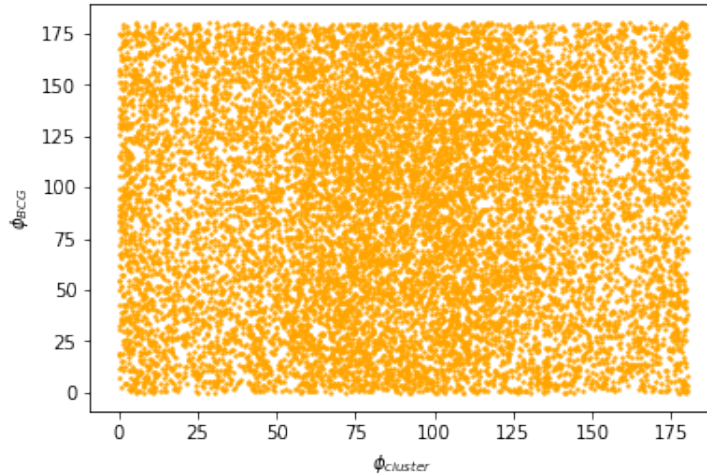


**Figure 3.18:** This scatter plot shows the  $\phi_{BCG}$  value plotted against the cluster phi value. One can see no obvious correlation between the angle of the BCG, and the angle of the cluster.

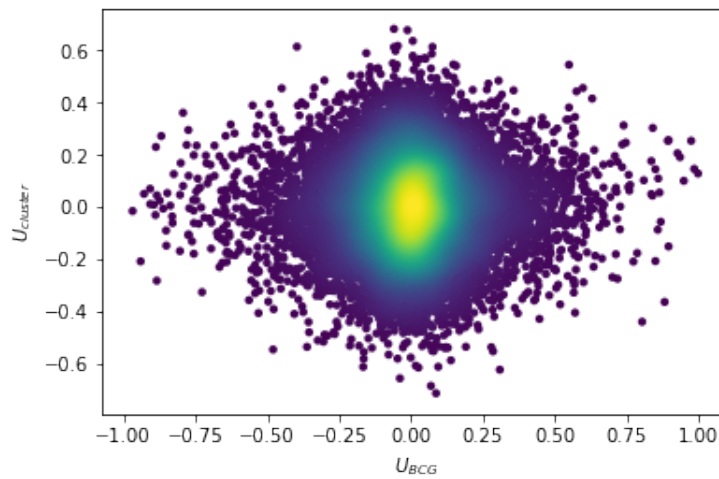


**Figure 3.19:** This shows a plot of the Stokes Parameter  $U$  of the BCG against that of the cluster.

## 3.6 Alignment

Following the convention established in Binggeli (1982) and Niederste-Ostholt et al. (2010), we define the alignment of the BCG and its host cluster as:

$$\Delta\phi \equiv |\phi_{BCG} - \phi_{cluster}| \quad (3.18)$$

and adopt their criteria that a cluster is considered to be aligned when  $\Delta\phi \leq 30^\circ$ .

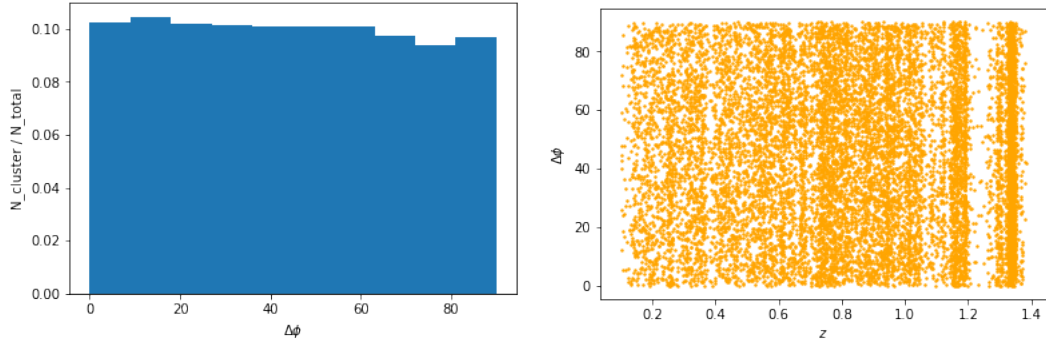


**Figure 3.20:** (Left) This histogram shows the alignment of the clusters with the BCG. This histogram is for the unfiltered data set (i.e: All 13373 clusters). The histogram is relatively flat, with no alignment apparent. (Right) A scatter graph of the alignment angle against redshift. There is no noticeable correlation to be seen in this graph either.

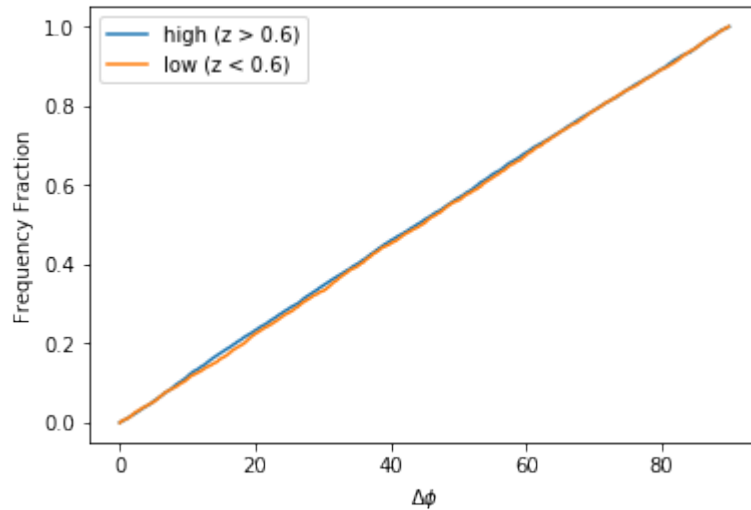


**Figure 3.21:** This shows the data represented as a normalised cumulative function. These graphs indicate that there is a negligible difference between the  $\phi$  values at low and high redshift.

We begin by plotting a histogram of the alignments in Figure 3.20a for all of the data points. As shown, this graph is relatively flat and suggests no tendency for any type of alignment. This is further exemplified by the scatter graph shown in Figure 3.20b.

Application of the Kolmogorov-Smirnov test in the case of  $\phi_w$  gives: statistic = 0.0169, p-value = 0.4296. The p-value is far higher than 0.1 (for 90% CL). As a

result, the difference between the low- $z$  distribution and the high- $z$  distribution is not statistically significant in this case (see Figure 3.21).

We then begin to select for clusters that are better for data analysis. We apply a strict criterion that the sample size of each cluster must be greater than 30 for use,  $\alpha < 0.8$  so that the cluster is not too round (so that the orientation is well-defined), and also that the redshift must be less than 0.8 to minimise the risk that we are looking at clusters with incorrect redshift values. This analysis is based in part upon viewing the histograms below (Figures 3.22 to 3.24).

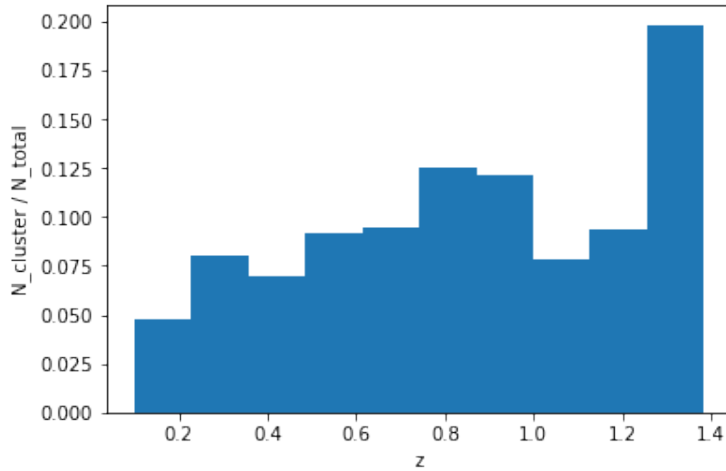


**Figure 3.22:** This is a histogram of the redshift of the clusters. As seen, a significant number of the clusters are at high redshift, with the modal bin being  $1.3 < z < 1.4$ . There is some debate as to whether the objects detected at these redshifts by HSC are actually at these redshifts, particularly given that the correlation between photometric and spectroscopic redshifts at higher redshifts. It is for this reason that we choose to deselect high-redshift clusters, to see if that significantly affects the histogram and correlation between alignment and redshift found.

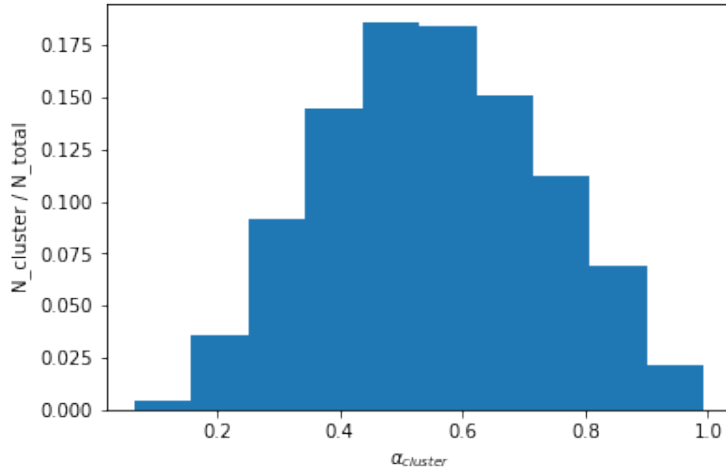


**Figure 3.23:** This is a histogram of the values of  $\alpha_{cluster}$ . As discussed earlier, the more rounded a cluster/BCG is, the more uncertainty there is in defining its angle. This histogram shows that we can deselect clusters with  $\alpha_w > 0.8$ , and still retain the majority of our sample.

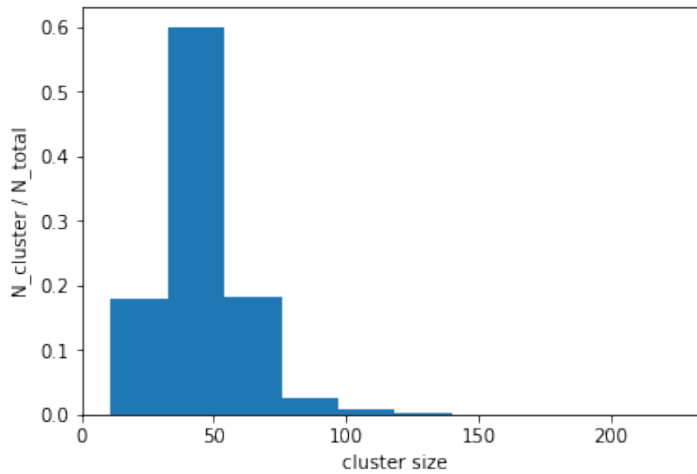


**Figure 3.24:** This is a histogram of the cluster size. The higher the sample size of a cluster, the lower the uncertainty of the  $\alpha$  and  $\phi$  values. From this, we can deselect clusters of size  $\leq 30$ , and still retain most of our sample.

Upon the application of these selection criteria, Figure 3.25 shows the new histogram, as well as the scatter plot for the alignment against redshift. As shown, there is no notable correlation between the alignment of the BCG and the cluster, and the redshift of these objects.

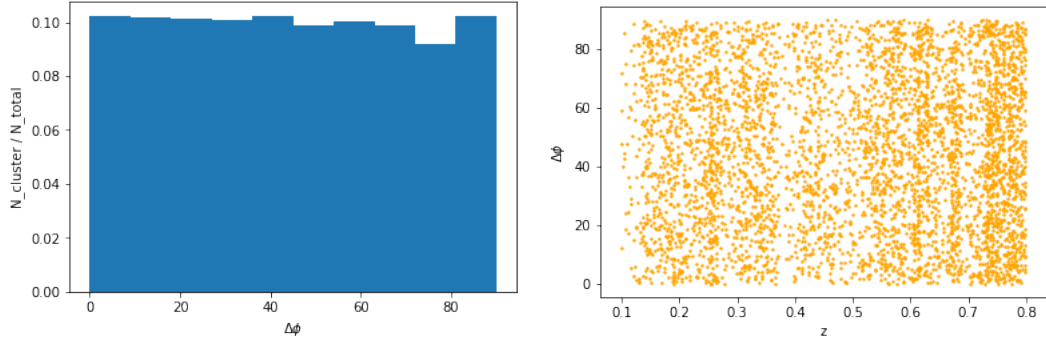


**Figure 3.25:** (Left) This histogram shows the alignment of the clusters with the BCG. This histogram is for the filtered data set. Again, there is no notable alignment. (Right) A scatter graph of the alignment angle against redshift, with no noticeable correlation.

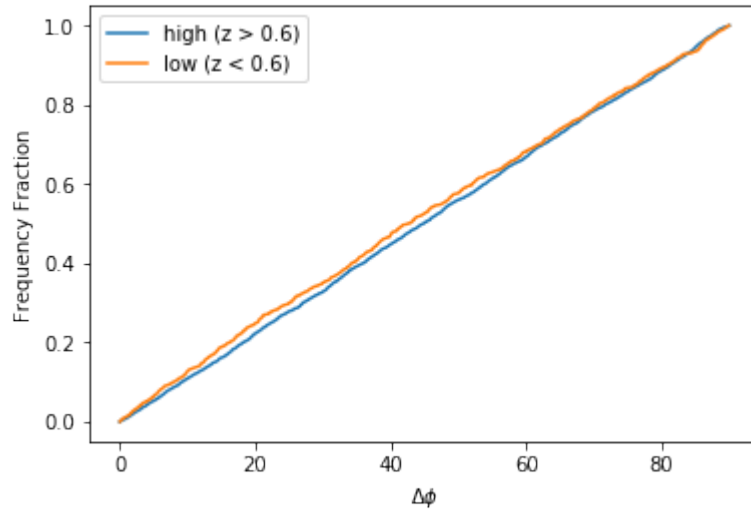


**Figure 3.26:** This shows the data represented as a normalised cumulative function. These graphs indicate that there is a negligible difference between the  $\phi$  values at low and high redshift, although it appears more significant than without the selection cuts.

Application of the Kolmogorov-Smirnov test in the case of  $\phi_w$  gives: statistic = 0.0327, p-value = 0.2772. The p-value is higher than 0.1 (for 90% CL). As a result, the difference between the low- $z$  distribution and the high- $z$  distribution is not statistically significant in this case, although it is an improvement compared to the data without the selection criteria (see Figure 3.26).

### 3.7 BCG Dominance

Another issue investigated in the Niederste-Ostholt et al. (2010) paper is the effect of BCG dominance with alignment. Both Kim et al. (2002) and Niederste-Ostholt et al. (2010) argue that it is worth investigating a connection between dominance and alignment because the method by which a BCG becomes more dominant could be connected to the method by which alignment is expected to occur. Following that paper, we define a measure of the dominance following the convention in Tremaine & Richstone (1977):

$$dom = m_1 - \frac{m_2 + m_3}{2} \quad (3.19)$$

i.e: we define dominance as the difference between the magnitude of the BCG, and the average magnitude of the second and third brightest galaxies. We are specifically using the i-band magnitudes for this calculation, for the reason that the i-band has the highest signal-to-noise ratio, as well as the best seeing. Noting then that by the definition of the magnitude system used that  $m_1 < m_2 < m_3$ , then  $dom < 0$  by definition.

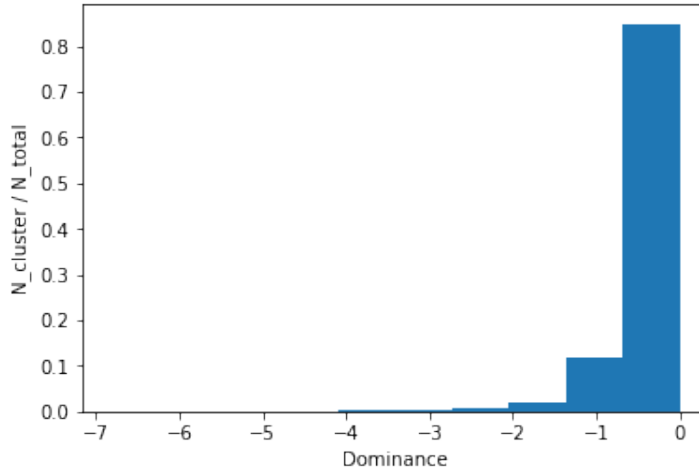


**Figure 3.27:** This is a histogram showing the measure of dominance. All values here are less than zero, precisely as expected.

Then, the histogram below shows the dominance with respect to redshift.

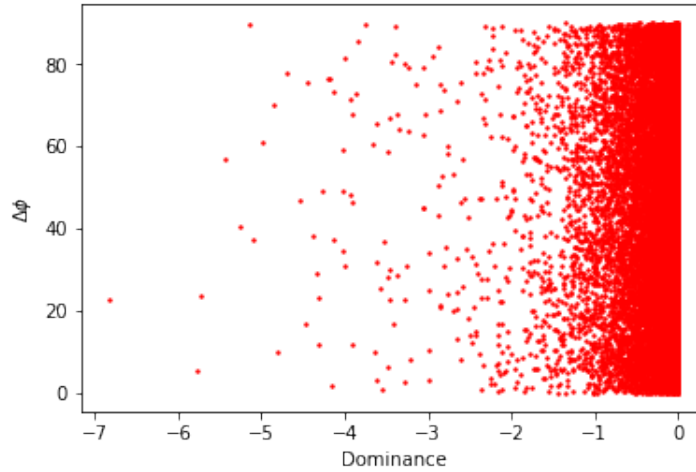


**Figure 3.28:** This scatter graph plots the relationship between BCG dominance and alignment. There is no obvious relationship between the two variables seen in this graph.

We note that there appears to be no correlation between alignment and dominance, although further work is recommended to further investigate the relationship between dominance and other variables. It is recommended that once the results on the alignments of the BCGs and their host clusters has been confirmed, then the effect of dominance can be further investigated.

# Chapter 4

## Conclusions

From this research a number of conclusions may be drawn. Firstly, we have shown that there is a statistically significant difference regarding the axial ratio of clusters between clusters of low- $z$  and clusters of high- $z$ .

However, the Binggeli effect has not been demonstrated in this paper; that is to say that the alignment of a BCG and its cluster appears not to have a redshift dependence. This is true even when various restrictions are placed on the clusters, such as ensuring the clusters are not too round so that uncertainty in  $\phi$  is reduced, ensuring that the sample size is sufficiently high enough so that it is less likely that individual galaxies heavily distort the shape and orientation of the cluster, and removing very high- $z$  clusters as a precaution since there is uncertainty as to whether these redshifts are accurate. There is additionally no correlation between dominance and alignment, although this is likely related to the absence of the Binggeli effect.

This result is highly surprising given the general consensus in the literature that the Binggeli effect exists, and its demonstration in recent papers (such as Niederste-Ostholt et al. (2010) that used a high number of clusters. In addition, this would also go against various theoretical models and cosmological simulations that favour the Binggeli effect. This suggests then that either there have been fundamental issues in these other papers, or there is a fundamental issue in this one. For example, it is plausible that there is some part of my code that effectively randomises the orientation or alignment angles, such as the angle corrections not

working as anticipated.

It is evident that more work needs to be completed in order to verify the results found in this paper. The next step in this project shall be to use the s19a v2 catalogue composed by Oguri which corrects for some issues regarding the high- $z$  clusters, though this is unlikely to significantly change the results of this paper given that we exclude clusters with  $z > 0.8$ . Testing how the results change upon additional fine-tuning of the selections may also be enlightening. An additional step is to check if the Niederste-Ostholt et al. (2010) paper can be replicated using the HSC data at  $0.08 < z < 0.44$ , particularly the difference in alignment between low- $z$  ( $z < 0.22$ ) and high- $z$  ( $0.22 < z < 0.44$ ).

# Appendix A

## Definition of $N_{cor}$ and $w$

The precise definitions of  $N_{cor}$  and  $w$  are given in Oguri et al. (2014). For completeness, that information is presented here.

To begin with, Oguri et al. (2014) seeks to determine where clusters exist in space using HSC data. Upon doing so, they then seek to quantify the probability that each galaxy of the cluster is actually in the cluster. To begin, they consider red-sequence galaxies (i.e: elliptical galaxies) because these are more likely to be found in clusters. One should also note that photometric redshifts are best measured for elliptical galaxies. To catalogue red-sequence galaxies, Oguri et al. (2014) quantifies the likelihood of each galaxy being a red-sequence galaxy at redshift  $z$  by:

$$\chi^2 = \sum_{i=1}^{N_{fil}} \frac{(m_{i,obs} - m_{i,SPS} - \delta m_{i,resi})^2}{\sigma_{m_{i,obs}}^2 + \sigma_{m_{i,resi}}^2} + \frac{(\log z_{11} - \log z'_{11})^2}{\sigma_{\log z}^2} \quad (\text{A.1})$$

where  $m_{i,obs}$  is the observed magnitude in the i-band,  $\delta m_{i,resi}$  is the error in magnitude associated with the i-band, and  $m_{i,SPS}$  is the magnitude associated with the stellar population synthesis (SPS) model. This  $\chi^2$  is effectively giving a rough determination of  $z$ . Then:

$$\frac{d\rho_\nu}{d\chi^2} = \frac{1}{2^{\frac{\nu}{2}} \Gamma(\frac{\nu}{2})} e^{-\frac{\chi^2}{2}} (\chi^2)^{\frac{\nu}{2}-1} \quad (\text{A.2})$$

with  $\nu = N_{fil} - 1$  (degrees of freedom)

$\frac{d\rho_\nu}{d\chi^2}$  gives the distribution in 3D space for determining the cluster. In effect, one should think about the determination of clusters in terms of the 2D data set not being 3D. HSC observes a number of galaxies at certain RA and DEC, but gives no clear indication of the depth of the galaxy. As such, when one views a set of galaxies that are close to one another in 2D space, it is possible that some of the galaxies seen there are in the foreground or the background, such that the predicted cluster is significantly different to what is expected. Thus Oguri et al. (2014) is trying to quantify whether a galaxy is both in the right (2D) position and the right redshift in relation to other galaxies, to see if they form a cluster.

This leads Oguri et al. (2014) to define a cluster member galaxy number parameter:

$$n_\nu(\chi^2) = \frac{2^{\frac{3\nu}{4}}}{\nu^{\frac{\nu}{2}} U\left(\frac{\nu}{4}, \frac{1}{2}, \frac{\nu^2}{8}\right)} \quad (\text{A.3})$$

with  $U(a, b, x)$  being the Tricomi confluent hypergeometric function given by:

$$U(a, b, x) = \frac{\Gamma(1-b)}{\Gamma(a+1-b)} \sum_{n=0}^{\infty} \frac{a^{(n)} z^n}{b^{(n)} n!} + \frac{\Gamma(b-1)}{\Gamma(a)} z^{1-b} \sum_{n=0}^{\infty} \frac{(a+1-b)^{(n)} z^n}{(2-b)^{(n)} n!} \quad (\text{A.4})$$

This parameter is normalised such that:

$$\int_0^\infty n_\nu(\chi^2) \frac{d\rho_\nu}{d\chi^2} d\chi^2 = 1 \quad (\text{A.5})$$

From this it is apparent that:

$$\left\langle \sum_{i=1}^{N_{mem}} n_\nu(\chi^2) \right\rangle = N_{mem} \int n_\nu(\chi^2) \frac{d\rho_\nu}{d\chi^2} d\chi^2 = N_{mem} \quad (\text{A.6})$$

Oguri et al. (2014) then selects galaxies based on their stellar mass range and their distance from the proposed centre of the cluster. The stellar mass filter is based on the fact that the luminosity of a galaxy is a function of its mass. If the luminosity of a supposed galaxy is much dimmer or brighter than expected, then it makes it far

less likely that it is actually a galaxy. As such, one should select galaxies within a particular mass range. The selected mass filter is given as follows:

$$F_M(M_{*,in}) = \exp\left[-\left(\frac{M_{*,in}}{M_h}\right)^4 - \left(\frac{M_l}{M_{*,in}}\right)^4\right] \quad (\text{A.7})$$

with  $M_h = 10^{13}M_\odot$  and  $M_l = 10^{10.2}M_\odot$ .

Furthermore, it is noted that the probability of a galaxy being in a cluster falls off from the centre of the cluster. To deal with this, a radius filter is given as follows:

$$F_R(R) = \frac{\Gamma[n/2, (R/R_0)^2] - (R/R_0)^n e^{-(R/R_0)^2}}{\Gamma(n/2, 0)} \quad (\text{A.8})$$

with the normalisation  $F_R(0) = 1$ , and Oguri et al. (2014) setting the parameters as  $n = 4$  and  $R_0 = 0.8h^{-1}$  Mpc.

From this, the richness map is as follows:

$$N_{mem}(\theta, z) = \sum_i n_\nu(\chi_i^2; \theta_i, z) F_M(M_{*,i}) F_R(D_A|\theta_i - \theta|) \quad (\text{A.9})$$

The next part of the calculation deals with masking. A masked region is an area of a survey in which there is no data, even though there has been a pointing to that patch of sky. There are various reasons as to why masked regions occur. Some are systematic, such as gaps between the CCDs on the telescope or gaps between pointings, and can be corrected for. Other factors may include poor weather conditions such as cloud factor. Thus the masking-corrected richness is given as:

$$N_{mem}(\theta, z) = \sum_i \frac{1}{f_{mask}} n_\nu(\chi_i^2; \theta_i, z) F_M(M_{*,i}) \times F_R(D_A|\theta_i - \theta|) \quad (\text{A.10})$$

where

$$f_{mask} = \frac{\int_{F_R>0} d\theta' S(\theta') F_R(D_A|\theta' - \theta|)}{\int_{F_R>0} d\theta' F_R(D_A|\theta' - \theta|)} \quad (\text{if } F_R(D_A|\theta' - \theta|) > 0) \quad (\text{A.11})$$

$$f_{mask} = \frac{\int_{F_R < 0} d\theta' S(\theta') F_R(D_A|\theta' - \theta|)}{\int_{F_R < 0} d\theta' F_R(D_A|\theta' - \theta|)} (\text{if } F_R(D_A|\theta' - \theta|) < 0) \quad (\text{A.12})$$

Oguri et al. (2014) imposes minimum values on the masking values. This is because as the masking area increases, the richness estimate becomes more uncertain.

With the clusters now determined, Oguri et al. (2014) goes back and determines the probability of each galaxy being a member of its cluster. Using a similar method as before, Oguri et al. (2014) looks for peaks in the 3D richness map  $N_{mem}(\theta, z)$ .

There are several details here that can be glossed over here, but essentially a weight is introduced to use high-significance cluster members to estimate a new cluster redshift. Then the BCG of the cluster is estimated (based on the brightness of the galaxy, whether it is a high significance galaxy in the cluster, and selected only if it is a red sequence galaxy). Then, a new cluster redshift is calculated based on the position of the BCG. The process of searching for the BCG and calculating redshifts, etc, is repeated until the solution (of maximising the likelihood) converges. From this, Oguri et al. (2014) assigns a weight factor as follows:

$$w_{mem} = n_\nu(\chi_i^2) F_M(M_{*,i}) F_R(D_A|\theta_i - \theta_{BCG}|) \quad (\text{A.13})$$

where  $D_A|\theta_i - \theta_{BCG}|$  is the physical distance between the BCG and the galaxy.

Finally, with the richness correction factor  $f_N(z)$  computed as:

$$f_N(z) = \frac{\int_{M_{*,cut}(z)}^{\infty} d\phi/dM_{*,in}(z_{ref}) dM_{*,in}}{\int_0^{\infty} d\phi/dM_{*,in}(z_{ref}) dM_{*,in}} \quad (\text{A.14})$$

where Oguri et al. (2014) set  $z_{ref} = 0.1$ .

Then the definition of  $N_{cor}$  as used in the catalogue becomes:

$$N_{cor} = \frac{N_{mem}}{f_N(z_{cl})} \quad (\text{A.15})$$

# Bibliography

- [1] Aihara H. et al., 2018, PASJ, 70, S4
- [2] Binggeli B. 1982, A&A, 107, 338
- [3] Bosch et al. 2017, (arXiv:1705.06766)
- [4] Ciotti L., Dutta S. N. 1994, MNRAS, 270, 390
- [5] Donahue, M., Ettori, S., Rasia, E., et al. 2016, ApJ, 819, 36
- [6] Donoso E., O’Mill A., Lambas D. G., 2006, MNRAS, 369, 1, 479
- [7] Dubinski J. 1998, ApJ, 502, 141
- [8] Faltenbacher, A., Gottloeber, S., Kerscher, M., Mueller, V. 2002, AA, 395, 1
- [9] Hashimoto Y., Henry J. P., Boehringer H., 2008, MNRAS, 390, 1562
- [10] Kim R. S. J., Annis J., Strauss M. A., Lupton R. H., 2002, in Borgani S., Mezzetti M., Valdarnini R., eds, ASP Conf. Ser. Vol. 268, Tracing Cosmic Evolution with Galaxy Clusters. Astron. Soc. Pac., San Francisco, p. 395
- [11] Siverd R. J., Ryden B. S., Gaudi B. S., 2009, preprint (arXiv:0903.2264)
- [12] Struble M. F., Peebles P. J. E., 1985, AJ, 90, 582
- [13] Niederste-Ostholt M. et al. 2010, MNRAS, 405, 2023-2036
- [14] Oguri M. 2014, MNRAS, 444, 147161
- [15] Oguri M. et al. 2018, ASJ, 70, SP1
- [16] Onuora, L. I., Thomas, P. A. 2000, MNRAS, 319, 614
- [17] Ulmer, M. P., McMillan, S. L. W., & Kowalski, M. P. 1989, ApJ, 338, 711
- [18] von der Linden A., Best P. N., Kauffmann G., White S. D. M., 2007 , MNRAS, 379, 867

- [19] Wang Y., Yang X., Mo H. J., Li C., van den Bosch F. C., Fan Z., Chen X., 2008, MNRAS, 385, 1511
- [20] West, M. J., De Propris, R., Bremer, M. N. & Phillipps, S. Ten billion years of brightest cluster galaxy alignments. Nat. Astron. 1, 0157 (2017).
- [21] York D. G. et al., 2000, AJ, 120, 1579

# Acknowledgements

I would like to thank my adviser Michael Strauss, for all of his support throughout this whole project. He has been a great source of wisdom, helping me to understand both the astrophysical concepts that I have applied, as well as the direction of this thesis as a whole.

I also thank my parents and family for being supportive throughout both my time at Princeton and my life in general, and for pretending to understand my thesis when I talk about it.

Within both the Astrophysics and Physics Department there have been many wondrous people with whom it has been a delight to work with. In particular, Madelyn Broome, Carlos Anicetti, Jacob Tyles, Hector Afonso Cruz, Elliot Davies, Aizhan Akhmetzhanova, Iryna Glushchenko, and Nicole Ozdowski are but just some of the noteworthy people who have helped through the long nights in Jadwin and Peyton. I extend this thanks to the numerous professors that have taught me throughout my Princeton career, be it in Physics, Russian, or any subject in-between, who have helped to facilitate my love of learning. I would also like to thank my roommate Arnold Mong, and all of the other great people that I have had the pleasure to know during my time at Princeton.

Additionally, there is no alternative but to thank the Quiz Bowl team for teaching me more about astrophysics than I would like to admit. Many thanks to Montagu James, Amy Tien, Jack Edmondson, Nathaniel Hull, Alice Egar, Eve Fleisig, Mason Tian, Jared Lockwood, and Ryan Golant.

Finally, I thank Amy Tien for being a wonderful source of support throughout, and for providing so much sunshine per square inch in my life.